This is a repository copy of *Noise characterization of patch antenna THz photodetectors*.

Noise characterization of patch antenna THz photodetectors

D. Palaferri[1,2 a)], Y. Todorov[1], D. Gacemi[1], S. Barbieri[1 b)], L. H. Li, [3] A. G. Davies,[3]
E. H. Linfield,[3] and C. Sirtori[1 a)]

[1]*Laboratoire Matériaux et Phénomènes Quantiques, Université Paris Diderot, Sorbonne Paris Cité, CNRS-UMS 7162,*

75013 Paris, France

[2]*Department of Electrical and Computer Engineering, The University of Texas at Austin, Austin, Texas 78758, USA*

[3]*School of Electronic and Electrical Engineering, University of Leeds, Leeds LS2 9JT, United Kingdom*

Current noise fluctuations have been investigated in terahertz (THz) quantum well photodetectors embedded in antenna-coupled photonic architectures, and compared with standard substrate-coupled mesa detectors. The noise measurements give a value of the photoconductive gain that is in excellent agreement with that extracted from previous responsivity calibrations. Moreover, our results confirm that the noise equivalent power (NEP) of the antenna-coupled devices is of the order of 0.2 pW/Hz$^{0.5}$. This low NEP value and the wide band frequency response (~ GHz) of the detectors are ideal figures for the development of heterodyne receivers that are, at present, a valuable technological solution to overcome the current limitation of THz sensors.

[a)] Authors to whom correspondence should be addressed: dpalaferri@utexas.edu , carlo.sirtori@univ-paris-diderot.fr
[b)] Present address: Institut d'Electronique de Microélectronique et de Nanotechnologie (IEMN), CNRS UMR 8520 Université de Lille 1, Avenue Poincaré B.P. 60069, 59652 Villeneuve d'Ascq, France

Quantum well infrared photo-detectors (QWIPs) have been demonstrated over the last 30 years to be fast and sensitive receivers in the mid- and far-infrared frequency ranges[1,2]. These optoelectronic devices are based on III-V semiconductor heterostructures, and most typically on GaAs/AlGaAs quantum wells (QWs). Their detection wavelength is set primarily by the QW width, as light absorption occurs through electronic transitions between two-dimensional QW states in the conduction band, called inter-subband (ISB) transitions. Device optimization is controlled through judicious choices of QW barrier thickness and Si doping[3] to minimize, respectively, the inter-well tunneling current and the thermally induced dark current. In 2005[4], H.C. Liu and co-authors reported QWIP devices operating at THz frequencies (1-10 THz) by employing low doping levels ($\sim 1\text{x}10^{10}\,\text{cm}^{-2}$) and low Al content in the barriers (1-5 %). These detectors have received special attention owing to their high responsivity ($\sim$ A/W)[4-9] and wide band frequency response ($\sim$ GHz)[9-10]. The coexistence of high sensitivity and high speed[11] is a unique property of QWIPs when compared to state-of-the-art THz receivers. Indeed, commercially available THz detectors with high detectivity (D*) such as hot-electron bolometers (D* $\sim 10^{10}$-10^{11} cmHz$^{0.5}$), Golay cells and DTGS crystals (D* $\sim 10^{9}$-10^{10} cmHz$^{0.5}$) are limited by their low response frequency (from few Hz up to tens of kHz)[12]. An ultra-fast THz detector would be beneficial in many applications including: broad wireless communication[13], the study of charge carrier dynamics in condensed matter[14], terahertz frequency imaging[15], frequency comb multi-heterodyne spectroscopy,[16] and ultra-fast laser research[17].

Recently, we have demonstrated a double metal patch-antenna array architecture[18,19] that significantly improves the responsivity and the thermal performances of a 5.4 THz QWIP (ref. [8]) with respect to the traditional 45° facet substrate-coupled geometry[1,4]. When using a 7 µm patch antenna-coupled microcavity device (the cavity size that gave the best performance), we reported an NEP = 0.18 pW/Hz$^{0.5}$ and a background-limited detectivity D*$_{BL}$=1.7x10^{11}cmHz$^{0.5}$/W at T = 4 K and 0.1 V. In the original work of H.C. Liu, considering the measured responsivity and background current and assuming a similar photoconductive gain, the mesa device has a detectivity D*$_{BL}$=3.5x10^{10}cmHz$^{0.5}$/W. Our enhancement in device performance is a consequence of the increased photonic confinement, the improved light coupling, and the strongly reduced dark current[20]. With the same photonic architecture, similar results have also been recently observed for a mid-infrared QWIP at λ=9µm[21]. However, a reliable calibration of performance requires noise current measurements in order to confirm the noise-equivalent-power and the detectivity values estimated from the responsivity and the dc background current. Interestingly, noise current fluctuations have been extensively investigated in mid-infrared QWIPs[22-26], but never for THz detectors.

Here, we report the current noise measurements for THz frequency ISB photodetectors, using the 5.4 THz QWIP structure of Ref. [8] processed both into a mesa structure with a 45° facet coupling and into a patch-antenna array. The resonant patch array devices (of size 7 µm) are found to have an NEP in the range 0.14-0.22 pW/Hz$^{0.5}$, whilst those in the mesa geometry are found to have an NEP in the range 0.6-1.3 pW/Hz$^{0.5}$. These values validate the ~five-fold performance improvement previously obtained using the values of background current and responsivity[8].

Three devices were used for the noise current investigation: a 400x400 µm^2 square mesa, and two 300x300 µm^2 patch-antenna arrays. The patch antenna devices can be categorised by their total number of patches N_{array} and the array unit cell $\Sigma=(s+a)^2$, where s is the cavity size and a is the distance between two neighboring patches. The parameters of the first resonant array device are N_{array}=196 and Σ=484 µm^2 (s=7 µm, a=15 µm), and those of the second array device are N_{array}=256 and Σ=361 µm^2 (s=9 µm, a=10 µm). The top-left panel of Fig. 1 shows an SEM image of the device illustrating the difference between the physical area $\sigma = s^2$ and the array unit cell Σ; the bottom-left panel depicts the biased two-level QW structure of the detector active region (E_1 and E_2 are the two subband energy levels). Details on the microfabrication and the MBE growth structure are given in Ref. [8]. A sketch of the experimental arrangement is shown on the right of Fig. 1: the THz QWIP devices are fed by a dc source and connected to a low-noise trans-impedance amplifier, femto DLPCA-200 (with a variable gain resistance $R_G = 10^3$-10^{11} Ω). The amplified ac noise current is measured using a signal analyzer, HP 89441A. Each measurement comprises the average of 100 acquisitions over the spectral range 10^2-10^6 Hz. The THz QWIPs are cryogenically cooled to liquid-He temperatures, and the detector chip covered with a cryo-shield at 4 K that is completely closed for dark current noise measurements and open, with a field of view FOV=60°, for background current noise measurements (as depicted in figure 1). The noise current spectral density (A/Hz$^{0.5}$), measured by the signal analyzer, includes noise contributions from the QWIP device, the dc source and the trans-impedance amplifier. By separating these noise components, as explained in the Supplementary Materials, it is possible to analyze the noise current of the THz detectors.

Figure 2 shows noise current spectral density measurements obtained by sweeping the voltage and temperature of the QWIP devices. Figures 2a and 2b show the noise current spectral density for the 7 µm and 9 µm cavity arrays, respectively, exposed to background radiation. As expected, the current noise increases upon increasing the applied voltage. We can identify three regions: a low frequency noise generated by external vibrations (100 Hz – 1 kHz), a plateau revealing the generation-recombination noise of the QWIP (1 kHz – 10 or 100 kHz), and the cut-off of the amplifier (100 kHz – 1 MHz; the cutoff

3

frequencies are f_c = 500 kHz and f_c = 400 kHz, for gain resistances $R_G = 10^6\ \Omega$ and $R_G = 10^7\ \Omega$, respectively, according to the amplifier data-sheet[27]). We note that ISB detectors do not typically show $1/f$ noise owing to the high quality of III-V materials and the low number of carriers involved[28]. Above 10 kHz for the 7 μm patch detector, and above 40 kHz for the 9 μm patch detector, we notice that the noise current increases as function of the frequency: this effect has been previously reported in the literature[29] and can be directly related to the capacitance (of a few tens of pF) of the coaxial cable, C_{BNC}, that connects the detector to the trans-impedance amplifier (see Supplementary Materials). The narrow peaks occurring above 100 kHz (mainly in figures 2a and 2c) originate from an external noise signal interfering with our electronic arrangement. Similar background current noise measurements have been acquired for the mesa device and are included in the supplementary material, together with the dark current noise measurements for the 9 μm cavity array.

Figure 2c illustrates the background current noise for the 7 μm cavity array device at a constant bias V_{QWIP} = 50 mV from T_{QWIP} = 4 K up to T_{QWIP} = 50 K. These temperature measurements have been acquired by employing different amplifier gains. The inset shows the dc background current $I_{bg}(T) = I_{photo} + I_{dark}(T)$, where I_{photo} is the photocurrent generated by the 300 K background and $I_{dark}(T)$ is the thermally activated dark current that increases exponentially with temperature. This set of I_{bg} curves was measured at the same temperatures as the noise curves. At low temperatures, the I-V curves show the step-like dependency on the voltage due to an ISB impact ionization effect[30], typically observed in THz QWIPs[8,30]. Following the theory of classic photoconductors[2,3], the noise current spectral density of THz QWIPs can be defined to be $i_n = (S_{GR} + S_T)^{0.5}$ with two distinct contributions: $S_{GR} = 4eg(I_{photo} + I_{dark})$ is the generation-recombination power spectral density (PSD) noise quantifying the electric charge fluctuation caused by random photogeneration and/or electronic transport dominated by scattering (g is the photoconductive gain); $S_T = 4k_B T_{QWIP}/R_{QWIP}$ is the Johnson-Nyquist noise, generated by the thermal fluctuations of charge carriers inside the QWIP active region (k_B is the Boltzmann constant and $R_{QWIP} = dV_{QWIP}/dI$ is the photodetector differential resistance). Regarding the generation-recombination noise PSD, several models have been reported for mid-infrared QWIPs[22-26] that mainly depend on the estimated value of the electron capture probability, p_c, in the well. As it will be demonstrated in the following analysis, THz QWIPs show $p_c \ll 1$, confirming the H.C. Liu model[23,25].

Fig. 2d illustrates the current noise for the 7 μm array device from background radiation (open symbols), extracted at 10 kHz from figure 2c. The green continuous line represents the total current noise i_n: the generation-recombination term, S_{GR}, is estimated from the dc current (inset of figure 3c) and the gain from the responsivity calibration of ref. 8; the Johnson-Nyquist

term S_T is obtained from the dc differential resistance of the device. The red dotted line and the black dashed lines show, respectively, the separated contributions of the thermal noise current $i_{n,T} = S_T^{0.5}$ and the dark current noise $i_{n,d} = (4eg I_{dark})^{0.5}$: in the latter case the dark current is written as $I_{dark} = I_0 \exp(-E_a/k_B T)$, where I_0 is a constant and $E_a = 16.5$ meV is the activation energy obtained by fitting dark current curves of several THz QWIP devices[31]. The orange dotted line indicates the background current noise $i_{n,ph} = (i_n^2 - i_{n,d}^2 - i_{n,T}^2)^{0.5}$. The crossing of this curve with the dark current noise sets the background-limited temperature, which corresponds at $T_{BLIP} = 21$ K[8] for this device. We notice that the background noise $i_{n,ph}$ increases as a function of temperature: this phenomenon, still under investigation, is attributed to an influence of the dark current on the photogeneration process, and will be discussed elsewhere. As expected, the generation-recombination term, S_{GR}, is the main contribution to the QWIP noise. At low temperatures ($T_{QWIP} \leq 10$ K), the detector performance is limited by the background-induced photocurrent noise, with the thermal and dark current noise representing a negligible contribution. Above T_{BLIP}, the QWIP device is dominated by dark current noise. The estimated total current noise based on the photoconductor model (continuous green line) accurately reproduces the noise measurements as a function of temperature within experimental error.

Fig. 3 presents the photoconductive gain of our THz QWIP devices as function of voltage at $T_{QWIP} = 4$ K. The continuous line is the gain obtained from the responsivity calibration of Ref. [8]: the triangular symbols correspond to the gain computed from the noise measurements of the 7 µm array device (fig. 2a); the square symbols refer to the 9 µm array device (open square symbols from fig. 2b and full square symbols from fig. S1b in the Supplementary Materials); and the circular symbols refer to the mesa device (fig. S1a). All noise measurements for this investigation are taken at 10 kHz (except for the dark noise of the 9 µm detector, which was measured at 1 kHz). The validity and consistency of the H.C. Liu model for noise currents in THz QWIPs is apparent from the Fig. 3 data, where the same gain values are obtained by interpreting two totally different measurements: responsivity[8] and PSD noise. The dashed line shows the capture probability $p_c = 1/g N_{QW}$, where $N_{QW} = 20$ is the number of quantum wells of the THz QWIP under study. Interestingly we can observe that over a large bias voltage range (25 meV < V < 100 meV), $p_c < 0.2$, which confirms the assumption that the noise in THz QWIPs can be treated in the same way as in classical photoconductors[2]. The linear increase of the photoconductive gain is typical for bound-to-quasi-continuum QWIPs[2] because the electron emission from the well is optimized and the drift velocity grows linearly under the relatively low electric field (0-0.6 kV/cm). An estimation of the drift velocity from our data is, however, unfeasible because of the uncertainty in the capture time for THz ISB detectors [ref. 2]. However, the high frequency response recently measured with THz QWIPs, of up to 6 GHz[9,10], suggests lifetimes of the order of a few ps (similar to mid-infrared QWIPs[2,21]), and confirms previous results obtained with a THz two-photon QWIP[11].

After analyzing the current noise PSD and the photoconductive gain, it is possible to quantify the photodetector sensitivity in both the mesa and patch antenna geometries. Fig. 4a shows the noise-equivalent-power (NEP) obtained from noise current measurements by using NEP = $i_n/\mathcal{R}$ where $\mathcal{R}$ is the measured responsivity for the mesa and the for the 7 μm cavity array devices. For the 9 μm array device, the responsivity has been calculated by knowing the gain and the absorption coefficient[8]. The open dots refer to the measured noise current values, whilst the continuous lines correspond to the estimates of NEP = $(4eg\mathrm{I_{bg}})^{0.5}/\mathcal{R}$ using the measured dc background current for each device. We observe an NEP ~ $0.14 - 0.22$ pW/Hz$^{0.5}$ for the 7 μm patch antenna array, which is five times smaller than that for the mesa device with NEP ~ $0.6 - 1.3$ pW/Hz$^{0.5}$. This significant reduction is a result of the strongly improved photon absorption in the antenna coupled detectors, which for the 7 μm array device has an estimated absorption, η_{array}, = 37 %, whilst for the mesa we quantify η_{mesa} = 5 %[8]. The 9 μm array device shows a higher NEP ~ $4 - 5$ pW/Hz$^{0.5}$ (corresponding to η_{array} = 13 %), which is due to the fact that the resonant modes TM$_{100}$ and TM$_{010}$ of these microcavities are largely detuned from the ISB transition (as shown in the responsivity spectra, reproduced on the same scale in the right insets of fig. 4a). Indeed the absorption coefficient of the patch-cavity photodetector is directly proportional to the overlap factor between the optical mode and the resonant absorption of the two-level QW[8,19]. It is, therefore, essential to tailor the parameters of the photonic architecture in order to optimize device performances: the antenna size s has to match the cavity, whilst the electronic resonances and the array spacing p maximize the fraction of photons coupled into the QWIP active region[20,21]. Using the measured NEP values, it is possible to calculate the background-limited specific detectivity, which is defined as D*$_{BL}$ = $(A_{det})^{0.5}$/NEP. We obtain D*$_{BL}$=$(1.4 - 2.3)$ x10^{11} cmHz$^{0.5}$/W for the 7 μm array device, D*$_{BL}$=$(0.6 - 1.4)$ x10^{10}cmHz$^{0.5}$/W for the 9μm array device, and D*$_{BL}$=$(2.3 - 5.0)$ x10^{10} cmHz$^{0.5}$/W for the mesa device, using the respective photodetector areas A_{det} = 9.5 x 10^4 μm^2 (7 μm cavity array), A_{det} = 9.2 x 10^4 μm^2 (9 μm cavity array) and A_{det} = 1.1 x 10^5 μm^2 (mesa). The detectivity values obtained from our measurement confirm the estimates that we reported previously[8].

Recently, optical heterodyne detection has been demonstrated as a tool to enhance quantum well photodetector performance[21]: this technique involves the coherent beating of a high power local-oscillator (LO) with a weak signal source on a fast detector. Employing a THz QCL as an LO[16, 32] with ~ 1 mW output power, and a weak THz source as the signal, it is possible to demonstrate[2,21] that the heterodyne NEP scales down to NEP$_{het}$ ~ $4eg/\mathcal{R}$ = 0.1 aW/Hz$^{0.5}$, which is orders of magnitude lower than what we obtain in dc, 0.2 pW/Hz$^{0.5}$. This ultra-high sensitivity devices, comparable to THz photon counters based on nano-bolometers[33], could be used, for example, to probe early universe THz radiation[34], or to assess the mutual coherence in THz laser frequency combs[35]. Moreover, a quantum well photodetector in an optical heterodyne system is highly convenient owing to its high frequency response[2,21]. Figure 4b shows the responsivity of the THz QWIP under study as a function of modulation

frequency[36,37]. For the 400 µm mesa, the 9 µm cavity array and the 7 µm cavity array devices, we find C_{mesa} = 19.1 pF, $C_{9µm}$ = 4.7 pF and $C_{7µm}$=4.3 pF, respectively, corresponding to cut-off frequencies f_{mesa}=167 MHz, $f_{9µm}$=682 MHz and $f_{7µm}$=748 MHz. Reducing the number of patches down to a 3x3 microcavity array could give a capacitance C_{3x3}=52.6 fF and a cut-off frequency $f_c \sim$ 60GHz, whilst a single microcavity could analogously give C_{1x1}=5.5 fF and a cut-off frequency $f_c >$ 100 GHz. These devices are therefore extremely promising candidates as high speed and large bandwidth receivers for THz wireless communications[13].

In summary, we have reported the noise measurements for THz QWIPs including a comparative study between standard mesa and patch-antenna architectures. The noise current spectral density measurements have confirmed a performances calibration of THz QWIPs in terms of responsivity. The microcavity geometry shows NEP values of the order of 0.2 pW/Hz$^{0.5}$. Future work will focus on investigating THz QWIPs in ultra-subwavelength resonators with strongly reduced current noise[20], and photovoltaic quantum cascade detectors[38] (operating at $\sim$ 0 V), that should further improve the performance of THz detectors.

Supplementary Materials. See supplementary materials for a description of the noise contributions in the electronic arrangement of Figure 1, the PSD noise measurements of the mesa device (under background exposure) and the 9 µm array (under dark), details of the noise measurements as function of the temperature of the 7 µm cavity in Figure 2.

REFERENCES

1) B. F. Levine, K. K. Choi, C. G. Bethea, J. Walker, and R. J. Malik, Appl. Phys. Lett. **50**, 1092 (1987).

2) Schneider, H. & Liu, H. C. in *Quantum Well Infrared Photodetectors: Physics and Applications* (Springer, 2007).

3) E. Rosencher & B. Vinter, *Optoelectronics* (Cambridge university press, 2004).

4) H. Luo, H. C. Liu, Song, C. Y., and Z. R Wasilewski, Appl. Phys. Lett. **86**, 231103 (2005).

5) M. Patrashin and I. Hosako, Opt. Lett. **33**, 168 (2008).

6) J. C. Cao and H. C. Liu, Semiconductors and Semimetals Vol **84**, 195 (2011).

7) R. Zhang, Z. L. Fu, L. L. Gu, X. G. Guo, and J. C. Cao, Appl. Phys. Lett. **47** 165101 (2014).

8) D. Palaferri, Y. Todorov, Y.N. Chen, J. Madeo, A. Vasanelli, L.H. Li, A. G. Davies, E.H. Linfield and C. Sirtori Appl. Phys. Lett. **106**(16), 161102 (2015).

9) B. Paulillo, S. Pirotta, H. Nong, P. Crozat, S. Guilet, G. Xu, S. Dhillon, L. H. Li, A. G. Davies, E. H. Linfield, R. Colombelli Optica **4**(12) 1451-1456 (2017).

10) H. Li, Wen-Jian W.-J. Wan, Z.-Y. Tan, Z.-L. Fu, H.-X. Wang, T. Zhou, Z.-P. Li, C. Wang, X.-G. Guo and J.-C. Cao Sci. Rep. **7** 3452 (2017).

11) H. Schneider, H.C. Liu, S. Winnerl, C.Y. Song, M. Walther and M. Helm Opt. Express **17**(15), 12279-12284 (2009).

12) A. Rogalski, F. Sizov, Opto-Electronics Review **19**, Issue 3 (2011).

13) T. Nagatsuma, G. Ducournau and C. C. Renaud Nat. Photonics **10**(6), 371 (2016).

14) R. A. Kaindl, M. A. Carnahan, D. Hägele, R. Lövenich and D. S. Chemla Nature 4**23**(6941), 734. (2003)

15) Z. Zhou, T. Zhou, S. Zhang, Z. Shi, Y. Chen, W.-J. Wan, X. Li, X. Chen, S. N. G. Corder, Z.-L. Fu, L. Chen, Y. Mao, J.-C. Cao, F. G. Omenetto, M. Liu, H. Li and T. H. Tao Adv. Sci. 5(7) 1700982 (2018)

16) Y. Yang, D. Burghoff, D. J. Hayton, J. R. Gao, J. L. Reno and Q. Hu Optica, 3(5), 499-502 (2016).

17) S. Barbieri, M. Ravaro, P. Gellie, G. Santarelli, C. Manquest, C. Sirtori, S.P. Khanna, E.H. Linfield, and A.G. Davies Nat. Photonics 5,5 306 (2011).

18) Y. Todorov, L. Tosetto, J. Teissier, A. Andrews, P. Klang, R. Colombelli,I. Sagnes, G. Strasser, and C. Sirtori, Opt. Express **18**, 13886 (2010).

19) Y. N. Chen, Y. Todorov, B. Askenazi, A. Vasanelli, G. Biasiol, R. Colombelli and C. Sirtori, Appl. Phys. Lett. **104**, 031113 (2014).

20) D. Palaferri, Y. Todorov, A. Mottaghizadeh, G. Frucci, G. Biasiol and C. Sirtori New J. Phys. **18**, 113016 (2016).

21) D. Palaferri, Y. Todorov, A. Bigioli, A. Mottaghizadeh, D. Gacemi, A. Calabrese, A. Vasanelli, L. Li, A. G. Davies, E. H. Linfield, F. Kapsalidis, M. Beck, J. Faist and Carlo Sirtori Nature **556**(7699) 85-88 (2018)

22) B. F. Levine, A. Zussmann, S. D. Gunapala, M. T. Asom, J. M. Kuo, and W. S. Hobson, J. Appl. Phys. 72, 4429 (1992).

23) H. C. Liu, Appl. Phys. Lett. **60**, 1507 (1992).

24) W. A. Beck, Appl. Phys. Lett. 6**3**, 3589 (1993).

25) C. Schonbein, H. Schneider, R. Rehm, M. Walther, Appl. Phys. Lett. **73** 1251 (1998).

26) R. Rehm, H. Schneider, C. Schoenbein and M. Walther Physica E 7 124–129 (2000).

27) Data-sheet FEMTO DLPCA-200 at https://www.femto.de/en/products/current-amplifiers/ (visited on 20/07/2018)

28) A. Delga, L. Doyennette, M. Carras, V. Trinité and P. Bois Appl. Phys. Lett. **102**.163507 (2013).

29) M. Ravaro, P. Gellie, G. Santarelli, C. Manquest, P. Filloux, C. Sirtori, J. F. Lampin, G. Ferrari, S. P. Khanna, E. H. Linfield, H.E. Beere, D. A. Ritchie and S. Barbieri IEEE Journal of Selected Topics in Quantum Electronics 19.1, pp. 8501011–8501011 (2013)

30) A. Delga, L. Doyennette, A. Buffaz, V. Berger, F.R. Jasnot, N. Péré-Laperne, L.-A. De Vaulchier, H.C. Liu J. Appl. Phys. 110, 013714 (2011)

31) D. Palaferri, Ph.D. thesis, University of Paris Diderot, Paris (2018)

32) H.-W. Hübers, S. G. Pavlov, A. D. Semenov, R. Köhler, L. Mahler, A. Tredicucci, H. E. Beere, D. A. Ritchie, and E. H. Linfield Opt. Express, **13**(15), 5890-5896 (2005).

33) J. Wei, D. Olaya, B. S. Karasik, S.V. Pereverzev, A. V. Sergeev and M.E. Gershenson. Nat. Nanotechnol. **3**(8), 496 (2008).

34) P.H. Siegel. In *Microwave Symposium Digest*, IEEE MTT-S International 816-819 (2010).

35) D. Burghoff, Y. Yang, Darren, J. Hayton, J.-R. Gao, J. L. Reno and Q. Hu Opt. Express 1190 23 2 2015

36) R. Saran and R. J. Curry Nat. Photonics **10**.2 81–92 (2016)

37) The frequency dependent responsivity is defined as (see ref. 36) $\mathcal{R}(f) = \mathcal{R}_{dc}/(1+(2\pi\tau_c f)^2)^{0.5}$ where $\mathcal{R}_{dc}$ is the dc responsivity and $\tau_c = R_{50\Omega}C_{QWIP}$ is the time response related to the frequency 3dB cut-off of the detector, including the 50 Ω output impedance ($R_{50\Omega}$) and C_{QWIP}, the QWIP electric capacitance

38) M. Graf, G. Scalari, D. Hofstetter, J. Faist, H. Beere, E. Linfield, D. Ritchie, and G. Davies, Appl. Phys. Lett. **84**, 475 (2004).
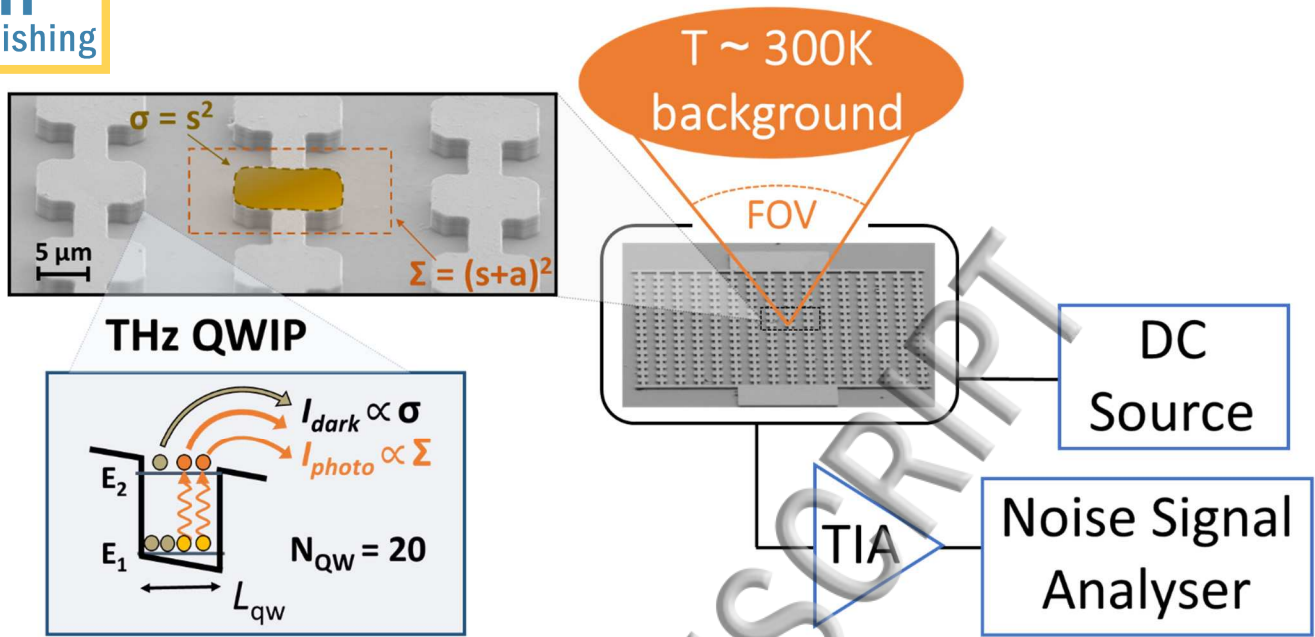
FIG.1: Electronic arrangement for noise current measurements. The upper left panel shows a scanning electron microscope image of the 9 µm cavity detector, whilst the lower scheme shows a two subband quantum well, together with the main sources of current.
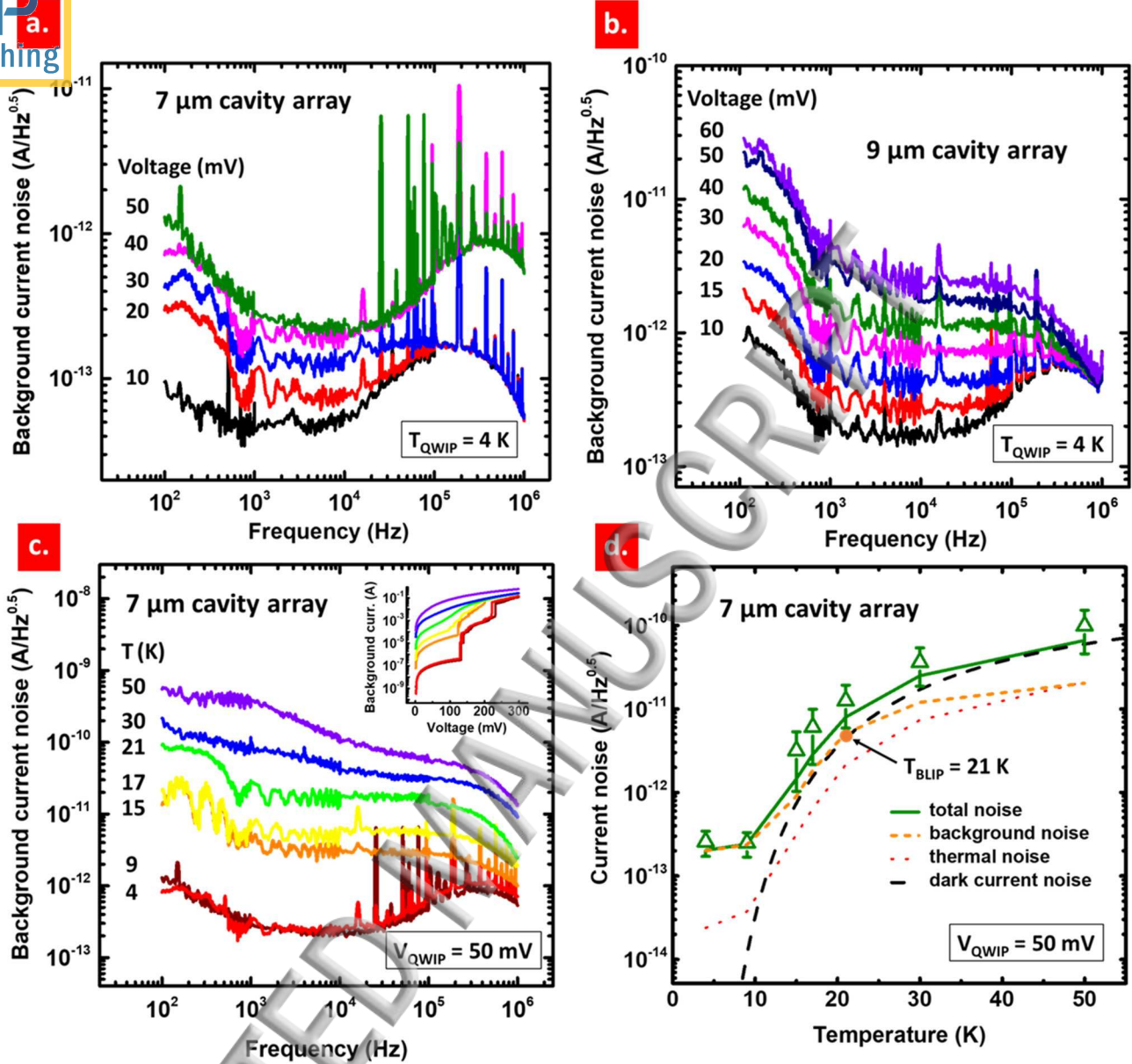
FIG.2: Current noise spectral density measurements for THz QWIPs under background exposure. The background current noise for (a) the 7 µm and (b) the 9 µm array devices at T=4 K are shown as a function of applied voltage and (c) the background current noise for the 7 µm array device is shown as a function of temperature at V=50 mV. The Resistance amplifier is 10^6 and $10^7\,\Omega$ for the 7 µm cavity array (a,c) and $10^6\,\Omega$ for the 9 µm (b). The inset in (c) illustrates the dc current-voltage characteristics of the 7 µm array device, measured at the same temperature of the acquired noise spectra. (d) Comparison between measured current noise for the 7µm cavity array QWIP at 10 kHz and the estimated total background noise (continuous green line). The dashed orange and black lines show respectively the background and dark current contributions. The dotted orange line represents the thermal noise contribution.
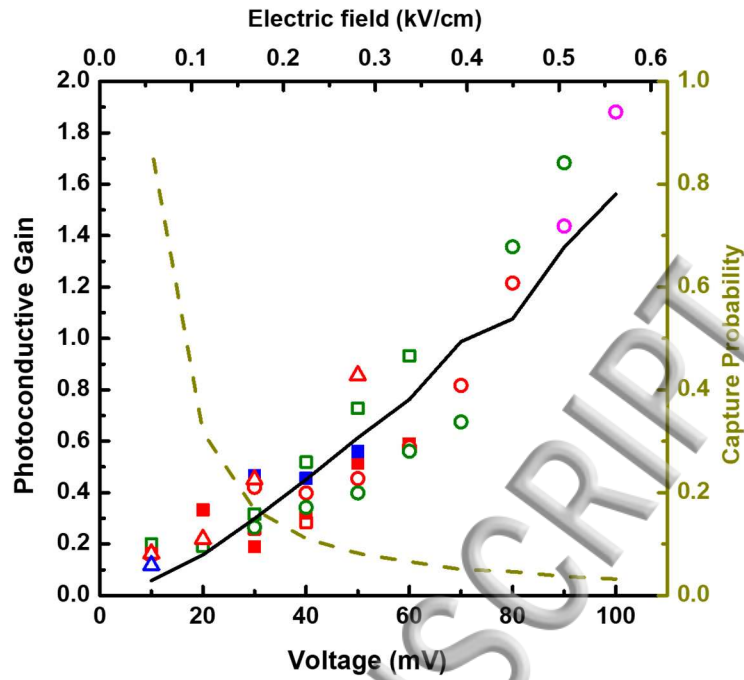
FIG.3: Photoconductive gain of the THz QWIPs. The continuous line shows the data from ref. [8] obtained from the responsivity; the circular, square and triangular dots correspond to the gain values obtained from the noise measurements of the mesa, 9 μm and 7 μm array devices, respectively. The dot colors correspond to specific amplifier gain values: pink = 10^5 Ω, green = 10^6 Ω, red = 10^7 Ω, and blue = 10^8 Ω. The dark yellow dashed line represents the electron capture probability in the QWs.
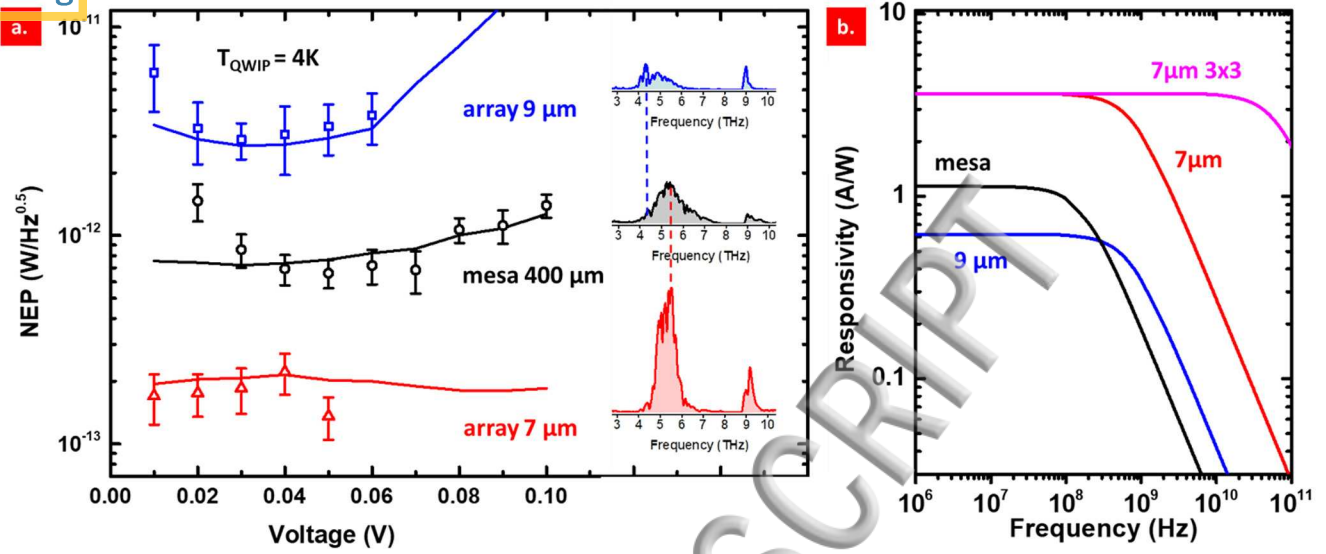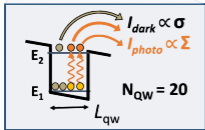
FIG.4: (a) NEP values of the THz QWIPs, both measured (open dots) and estimated from the IV characteristics (continuous line). The inset shows the respective responsivity spectra, reproduced from D. Palaferri at al. Appl. Phys. Lett. 106(16), 161102 (2015), with the permission of AIP Publishing. (b) Frequency dependence of the responsivities for the detector devices under study; the pink curve is referred to a 7μm antenna-coupled QWIP with a strongly reduced number of patches, i.e. a 3x3 array.
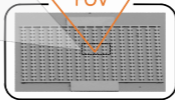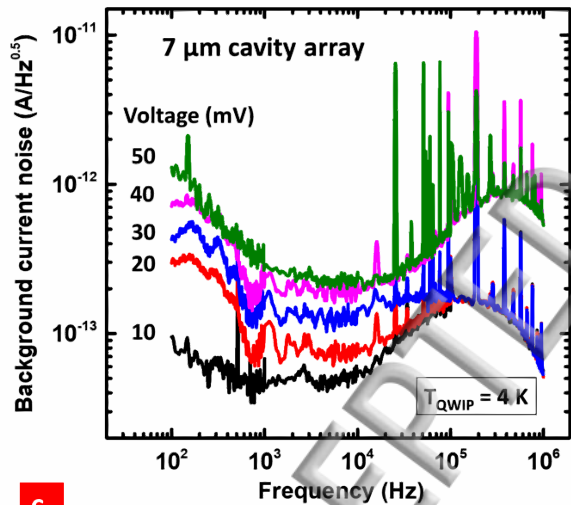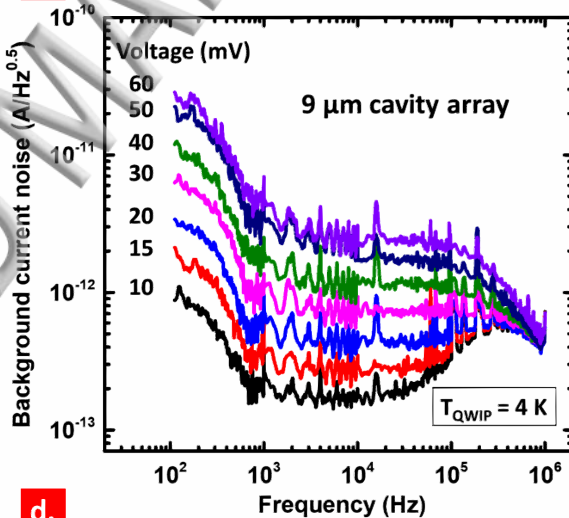
THz QWIP

$\sigma = s^2$

$\Sigma = (s+a)^2$

$5 \ \mu m$

T ~ 300K background

FOV

$I_{dark} \propto \sigma$

$I_{photo} \propto \Sigma$

E_2

E_1

$N_{QW} = 20$

L_{qw}
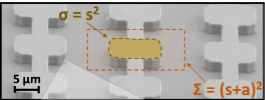
DC Source

TIA

Noise Signal Analyser

a. 7 μm cavity array

Voltage (mV): 50, 40, 30, 20, 10

T_{QWIP} = 4 K

b. 9 μm cavity array

Voltage (mV): 60, 50, 40, 30, 20, 15, 10

T_{QWIP} = 4 K

c. 7 μm cavity array

T (K): 50, 30, 21, 17, 15, 9, 4

V_{QWIP} = 50 mV

(inset) Background curr. (A) vs Voltage (mV)

d. 7 μm cavity array

T_{BLIP} = 21 K

— total noise
— — background noise
······ thermal noise
— — dark current noise

V_{QWIP} = 50 mV

a. $T_{QWIP} = 4K$

NEP (W/Hz$^{0.5}$)

array 9 µm

mesa 400 µm

array 7 µm

Voltage (V)

Frequency (THz)

b.

Responsivity (A/W)

7µm 3x3

mesa

7µm

9 µm

Frequency (Hz)